Marine Geology 434 (2021) 106431

Contents lists available at ScienceDirect

Marine Geology

journal homepage: www.elsevier.com/locate/margo

Episodicity of structural flow in an active subduction system, new insights from mud volcano's carbonate veins – Scientific Ocean drilling expedition IODP 366

Emanuelle Frery [a,*], Patricia Fryer [b], Walter Kurz [d], Ai Nguyen [c], Olivier Sissmann [e], Tonguc Uysal [c], J. Zhao [c]

[a] CSIRO, 26 Dick Perry avenue, Kensington, WA 6152, United States of America
[b] Hawaii Institute of Geophysics and Planetology University of Hawai'i, Mānoa 1680 East-West Road, POST #514, Honolulu, HI 96822, United States of America
[c] School of Earth and Environmental Sciences, The University of Queensland, St Lucia, QLD 4072, Australia
[d] Institute of Earth Sciences, University of Graz, Heinrichstrasse 26, Graz A-8010, Austria
[e] IFP Energies nouvelles 1 & 4, Avenue de Bois-Préau 92852, Rueil-Malmaison Cedex, France

ARTICLE INFO

Original content: Cyclicity of structural flow in an active subduction system, new insights from mud volcano's carbonate veins – Scientific ocean drilling expedition IODP 366- dataset (Original data)

Keywords:
Fault sealing
Mud volcano
Fluid circulation pathway

ABSTRACT

This study's goal is to understand the structural events and episodes of fluid flow recorded in calcium carbonate precipitation sampled in Mariana forearc serpentine mud volcanoes. Those active mounts provide a unique window to deep structural and fluid flow events affecting the subduction channel mélange zone and the subducted Pacific Plate.

To build a conceptual model of vein precipitations from the subduction zone to the mud volcanoes edifice, we unravelled the origin, timing, and mechanisms of those precipitations with a multidisciplinary study of calcium carbonate veins, from samples drilled in the flank of Fantangisña Seamount during the International Ocean Discovery Program (IODP) Expedition 366.

Structural analysis of the carbonate vein network revealed stages of precipitation and dissolution. The most ancient calcium carbonate minerals underwent high tectonic stress and several degrees of silicification. U-Pb dates ranged from Early Cretaceous to present day, recording potential pre-convergence events and calibrating an episodic building of the Mariana mud volcanoes from the start of the convergence to present day. The UCC-normalized LREE pattern, $^{87}Sr/^{86}Sr$ ratios ranging from 0.704977 to 0.705798 and $\delta^{18}O$ signature 18.7 to 19.8 (‰, V-SMOW) of the veins indicate a mixed origin of the precipitated fluids influenced by the serpentine mud signature.

Those mud volcanoes were episodically built from the start of the subduction to present day in function of the forearc tectonic activity. They are complex systems internally composed of a fault network providing multiple circulation pathways that can be successively opened or closed.

1. Introduction

Brittle fault transmissivity varies through the seismic cycle (Sibson, 1994), the fluid pressure evolution being controlled by fluid flow and rapid compaction (Byerlee, 1990; Rice, 1992; Sleep and Blanpied, 1994) or pressure solution crack sealing processes (Renard et al., 2000; Gratier et al., 2002). Faults are complex zones, with internal variations of lithology and architecture that are function of the fault evolution stage, i.e. from relay zones to faulted rocks (Childs et al., 2009). These parameters also greatly influence fault zone hydro-mechanical properties and behaviors (Faulkner and Rutter, 2001).

Numerous U-Th radiogenic datings and isotopic studies of Quaternary calcium carbonate veins precipitated within faults zones have shown that those veins are a relevant proxy for calibrating both tectonic and paleo-hydrothermal activity (Uysal et al., 2007; Dockrill and Shipton, 2010; Nuriel et al., 2017; Uysal et al., 2011; Frery et al., 2015; Vignaroli et al., 2016). Recent U-Pb calcium carbonate geochronology applied to older calcium carbonate veins increased the range of possible radiogenic datings up to Palaeozoic ages. Single deformation events were successfully constrained (Roberts and Walker, 2016; Ring and

* Corresponding author.
E-mail address: emanuelle.frery@csiro.au (E. Frery).

https://doi.org/10.1016/j.margeo.2021.106431
Received 13 October 2020; Received in revised form 2 December 2020; Accepted 7 January 2021
Available online 29 January 2021

Gerdes, 2016; Nuriel et al., 2017) as well as complex deformation events in sequences of orogenic forelands events (Hansman et al., 2018; Beaudoin et al., 2018).

Here, the challenge is to understand the origin of calcium carbonate precipitation events recorded in Mariana forearc serpentine mud volcanoes as to better calibrate the seismic cycle of this region. The samples examined are pebble veins embedded in serpentinite mud and the veins' orientations cannot be directly related to given tectonic events (Fryer et al., 2018; Fryer et al., 2020). In order to assess the cycles of calcium carbonate precipitation in such a system, we need to unravel (i) the time-lapse, duration, recurrence and (ii) mechanisms of precipitation as well as (iii) the source of the precipitation fluid and the circulation trigger.

We undertook a structural, geochemical and radiogenic study of calcium carbonate veins sampled on the flank of Fantangisña Seamount during the International Ocean Discovery Program (IODP) Expedition 366 and proposed a conceptual model of the calcium carbonate vein precipitation from the subduction zone to the mud volcano edifice.

2. Mariana forearc active mud volcanoes

Mariana forearc serpentinite mud volcanoes (Fig. 1A) provide a window to deep structural and fluid flow events affecting the subduction channel mélange zone and the subducted Pacific Plate. These active mud volcanoes are located between the trench and the active volcanic arc on the eastern edge of the Philippine Sea plate, within 100 km west of the non-accretionary Mariana convergent margin (Uyeda and Kanamori, 1979).

Recent exploration of these mud volcanoes revealed varying thermodynamical conditions at different slab depths, as well as the mechanisms of material subduction and exhumation through deep-rooted faults, from the slab and subduction channel mélange zone to the sea floor. The Ocean Drilling Program (ODP) Leg 125 and Leg 195 (Fryer et al., 1992; Salisbury et al., 2002) drilled Conical and South Chamorro Seamounts located far from the trench (about 78 km) with a deep plate interface (up to 18–19 km), providing a window into warm (~350 °C) subduction conditions. The IODP expedition 366 explored Asùt Tesoru, Fantangisña, and Yinazao Seamounts, located closer to the trench, respectively about 72 km, 62 km, 55 km to the west of the trench, with a shallower inferred subducted slab 18 km, 14 km, 13 km below the volcanoes summit and with temperatures of the slab-mantle interface below the above-mentioned three seamounts ranging from ~250 to 80° (Fryer et al., 2018, 2020). While those mud volcanoes were informally known as Big Blue, Celestial and Blue Moon Seamounts, the IODP expedition 366 scientific party agreed on using their Chamorro names.

The seamounts are composed of unconsolidated flows of serpentine mud with ultramafic clasts, mainly serpentinized mantle peridotite (Fryer and Salisbury, 2006), and reveal active fluid seepage of slab derived fluids (Fryer et al., 1999, 2006). This study focusses on Fantangisña Seamount flank and summit drilling (Fig. 1B) material sampled during IODP expedition 366. This mud volcano lies at the northern edge of a north-western trending uplifted ridge and is located along a northeast trending lineament. Several stages of slumps were indicated at the summit (Oakley et al., 2008); alkalinity and Mg analyses of pore fluids from the summit indicated a slow discharge of a deep sourced fluid into the serpentine mud matrix.

3. Sampling and methods

The recovered material mainly consists of serpentinite mud containing lithic clasts derived from the underlying forearc crust/mantle and the subducting Pacific plate slab. Clasts derived from the underlying forearc crust and mantle and the subducted slab form a major fraction of the recovered clasts at the studied sites: U1497 (Fantangisña summit) and U1498 (Fantangisña flank). Site U1497 drilling reached depths at Fantangisña Seamount summit (Fig. 1B) between 2018.30 and 2019.24 mbsl, recovering 42.38 m of material. Site U1498 is located on the flank of the edifice, drilling between 3284.70 and 3496.21 mbsl and recovering 103.41 m of core (Fryer et al., 2017).

This work focuses on carbonate veins sampled at the contact between a metabasite and a chert limestone (Fig. 2), in cores U1498A 3R 2 W,

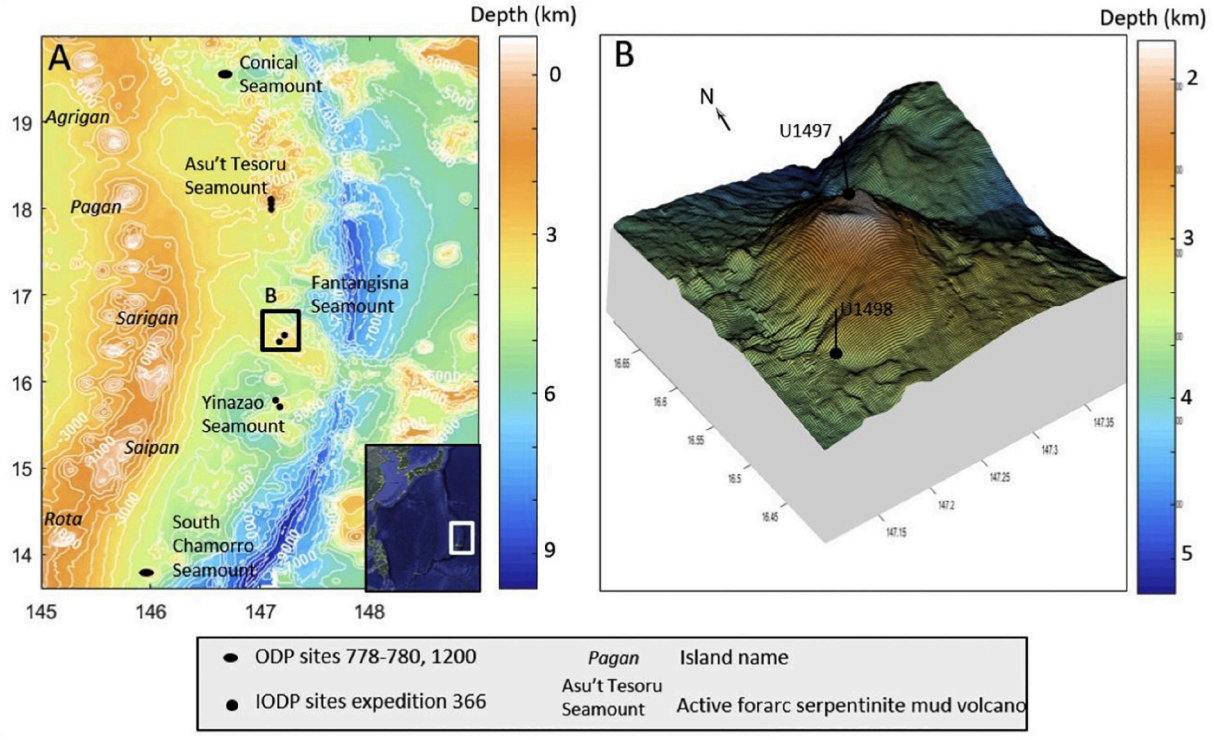

Fig. 1. Bathymetry of the Mariana forearc showing the locations of the serpentinite mud volcanoes dated with U-Pb method. (B.) Detailed bathymetry and location of IODP 366 sites on the flank and summit of Fantangisña (Celestial) Seamount.

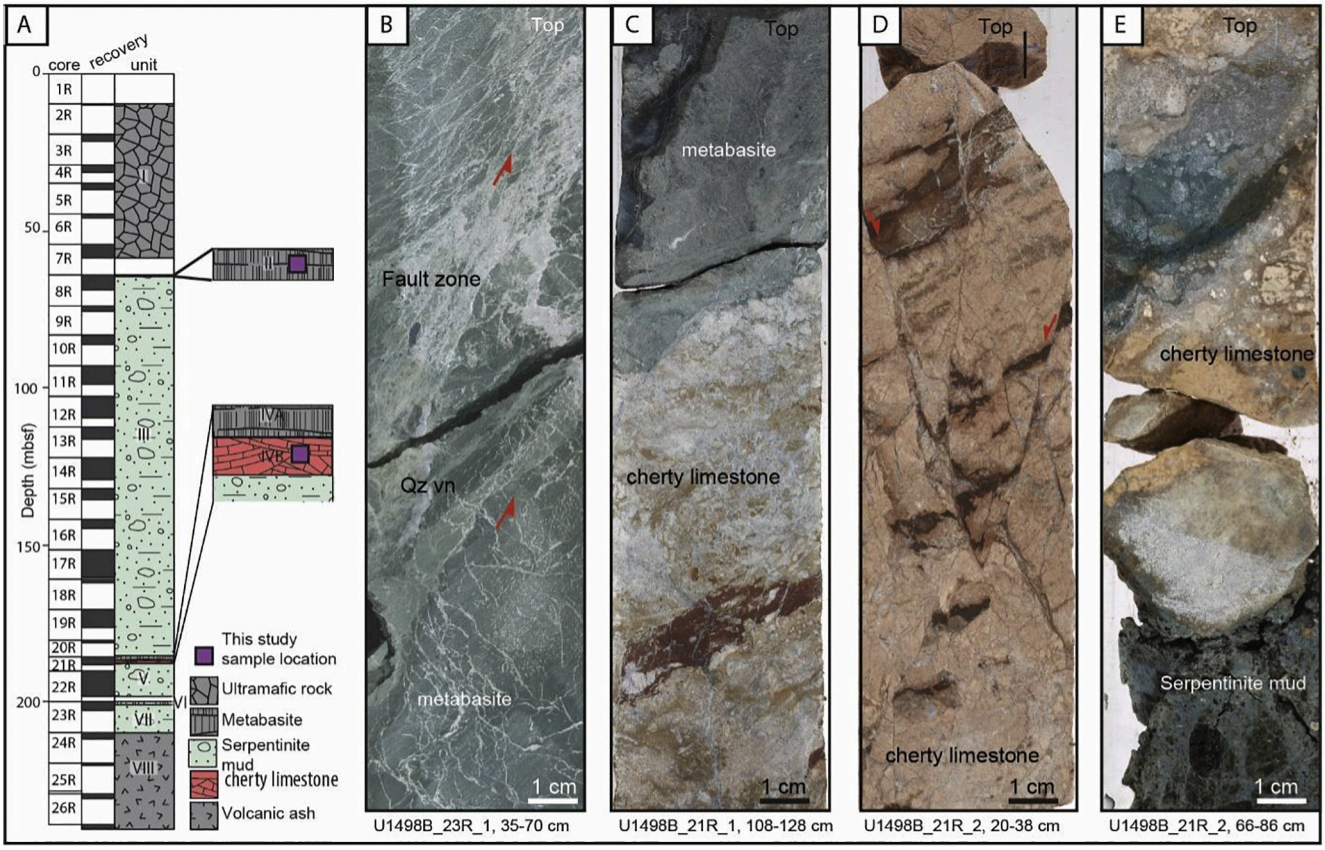

Fig. 2. Location and lithology of this study carbonate vein samples (A) location of the metabasite and metasediment sequences within the pebbly serpentine mud on the example of Hole U1498B. (B–E) Close up pictures of this sequence.

U1498B-8R and U1498B-21R through U1498B-23R. This hard rock sequence is embedded in pebbly serpentinite mud. Following a macroscopic structural analysis of the vein network on-board (Fryer et al., 2017, 2018), the various carbonate vein families were sampled so as to describe the mineral growth mechanisms and diagenesis processes. Polished thin sections and slabs were respectively imaged with a petrographic microscope and microbeam X-Ray Fluorescence (XRF) (Bruker M4 TORNADO™) imaging. Scanning electron microscopy (SEM) picking of the mineral content led to subsamples from 7 rock slabs for U-Pb absolute dating by laser-ablation.

3.1. Trace elements

Trace elements of calcium carbonate veins of polished slabs were measured using an ASI RESOlution 193 nm excimer UV ArF laser ablation system with a dual-volume Laurin Technic ablation cell integrated with a Thermo iCap RQ quadruple mass spectrometer at The University of Queensland Centre for Geoanalytical Mass Spectrometry, Radiogenic Isotope Facility, following Ubide et al., 2019's protocol with some modifications for spot analysis. To eliminate contaminants from lapidary process, the polished slabs were thoroughly cleaned with soap solution, followed by MilliQ water with assistance of a sonication, and dried overnight at 60 °C on a hot plate before loading into the ablation cell. The mass spectrometer was tuned by scanning a NIST612 glass reference material with a laser parameters of 50 μm spot size, a 3 μm/s speed, and a 10 Hz repetition rate, to achieve an optimal condition of high sensitivity and low double charge and oxide rates. Sample ablation was performed with a laser beam of 3 J/cm^2, a spot size of 100 μm, and a repetition rate at 10 Hz. The ablated sample aerosols were directed to a funnel and carried to the mass spectrometer by a mixture of ultrapure He (350 ml/min), Ar (950 ml/min) gases. A minor amount (5 ml/min) of N_2 gas was also added to the gas system for boosting transport efficiency and elemental intensity. The acquisition time for each spot was 20s for the baseline, 25 s for sample ablation, and 10s for system washout. The sample spots were run in between the glass standard NIST 614 which was used as a calibration standard for data reduction using Iolite 3.6 (Woodhead et al., 2008). Calcium was assumed to be 40% in the samples and used as an internal standard for data normalization. Some of NIST 614 spots were processed as unknowns during data reduction and their elemental concentrations agree well with certified values (errors of rare earth elements, Rb, Sr, Ba, Th and U within 5% and of other elements ~10%).

3.2. U/Pb dating

U/Pb data were obtained from Nu II instrument Multi-collector Inductively Coupled Plasma Mass Spectrometer coupled with the same laser ablation system. The sample zone with high U and low Pb, based on the trace element data, were ablated at a spot size of 100 μm, a repetition rate of 10 Hz and a fluency of 3 J/cm^2. The data were acquired for 20s for the baseline, 30s for sample ablation, and 10s for system washout before the next spot analysis. The induced sample aerosols were carried by ultrapure He and Ar gases and a trace amount of N_2 gas to stabilize the aerosol input to the plasma. The ^{238}U was measured with Faraday cups and ^{208}Pb, ^{207}Pb, ^{206}Pb, and ^{204}Pb were measured on four ETP discrete-dynode electron multipliers. We have obtained ~150 spot analyses on in-house calcite standards (AHX-1A and ASH15E), ~270 spot analyses on the selected samples and ~ 80 spot analyses on NIST-614 glass standard for U-Pb isotope analyses. U-Pb isotopic ratios and their uncertainties were calculated using Iolite 3.6 (Paton et al., 2010). ^{238}U/^{206}Pb and ^{207}Pb/^{206}Pb ratios were corrected for any instrument drifts and isotopic fractionation (but not corrected for down-hole

fractionation) using the glass standard NIST 614 values. The corrected U-Pb isotopic data of calcite standard AHX-01A was plotted on Tera-Wasserburg concordia using an Isoplot software to calculate its age. The "true" age of this standard is 209.8 ± 1.3 My (it is the average age obtained by being multi-calibrated against ASH-15E, with age of 3.001 ± 0.0012 My by ID-TIMS). An offset factor of the measured age vs. true age of AHX-1A was used to normalise the $^{238}U/^{206}Pb$ ratios of the unknowns, including ASH-15E. The normalized U-Pb ratios of all samples and standards were regressed on Tera-Wasserburg concordia to achieve the ages. The ASH15E gives an age of 3.021 ± 0.051 My, within an error of the published value (Nuriel et al., 2017), suggesting the cross-calibration is reliable.

A careful check of those data refined the U/Pb dating dataset by laser-ablation to four samples. The samples' IODP references are U1498B 8R 1 W(10 to 12 cm), U1498B 21R 2 W(6 to 10 cm), U1498B 21R 2 W(26 to 29 cm), U1498A 3R 2 W(10 to 12 cm). To simplifies the text, they are here respectively called A5, A1, A7 and D5. The other samples have U content too low for analysis (U < 0.01 ppm) and/or U/Pb ratios so small ($^{238}U/^{206}Pb$ < <10) that they imply huge amount of common Pb. In comparison, zircons typically have uranium content of ~50–500 ppm (1000–10,000 times higher than most calcites) and U/Pb ratios far in excess of 10 for samples younger than 50 My.

3.3. Strontium, carbon and oxygen isotopes

Strontium isotope ($^{87}Sr/^{86}Sr$ ratios) analysis were performed at the Radiogenic Isotope Facility, University of Queensland, Australia. ~10 mg of sample powder was obtained from each calcite vein and digested in weak acetic acid to extract Sr from the carbonate phase. The sample solution went through a Sr separation following standard cation exchange column procedure as detailed in Wei et al. (2014). 87Sr/86Sr was measured using a Nu Plasma I multi-collector inductively-coupled plasma mass spectrometry (MC-ICPMS). A standard SRM 987 was measured at every five samples and used as an external calibration. Long-term repeated measurement of the SRM 987 standard yields a mean 87Sr/86Sr value of 0.710250 ± 0.000032 (2σ).

The $\delta^{13}C$ and $\delta^{18}O$ isotopic composition of carbonate samples were measured at the NGL Geochemistry laboratory at CSIRO Energy on a Thermo MAT253 IRMS, coupled with a dual inlet connected to a Gasbench II. For each sample, a few milligrams of powder was placed in a glass vial capped with a septum, which was then flushed with Helium. Orthophosphrous acid was then injected into the flushed vial, dissolving the carbonate powder and releasing CO_2 within the vial. The CO_2 gas was then sampled automatically from the vial headspace by a syringe and sent to the IRMS, where isotopes abundances were measured on masses 45/44 (for $\delta^{13}C$) and 46/44 ($\delta^{18}O$). Values of $\delta^{18}O$ V-PDB were converted to $\delta^{18}O$ V-PDB to $\delta^{18}O$ V-SMOW according to $\delta^{18}O$ (V-SMOW) = 1.03092[$\delta^{18}O$(V-PDB)] + 30.92 (Coplen, 1995).

4. Results

4.1. Structural analysis

On-board structural analysis of the cores revealed simple to multiple veins within the ultramafic clasts. Those veins are mainly composed of serpentine minerals and occasionally of carbonate, silicate or brucite (Fryer et al., 2018). Carbonate and silicate veins were mostly recovered within cataclasites and fault zones that cross-cut a unit composed of a metabasite and a cherty limestone embedded in the serpentinite mud (Fig. 2). A dense network of millimetre- to centimetre-wide veins cross-cut the metamorphosed volcanic rock, especially around a normal fault zone located in U1498B-23R-1 (Fig. 2B). Above it, a primary contact, dipping at 5° to 30°, is preserved between the metabasite and the metamorphic limestone (Fig. 2C); the latter is brecciated (Fig. 2D,E) and subsequently sheared along conjugate high-angle normal faults.

Multi-elemental XRF mapping and SEM analyses of the polished slabs A5, A1, and A7 outline several composite veins made of calcium and silicates (Fig. 3, Table 1, Table 2,Table 3). Three vein sets on A5 (Fig. 3A) show a progressive silicification of the primary calcium carbonate from dominant calcium carbonate in vein v1 (> 50% CaO, Table 1) to dominant silica in vein v3 (>50% SiO_2,Table 1). Two types of veins were imaged on A1 (Fig. 3B). Wide (>0.5 cm) calcium carbonate veins (v1, > 90% CaO, Table 2) are brecciated and displaced along conjugate high-angle faults. A few millimetre (~0.5–1 mm) silica dominated veins (v2, >50% SiO_2,Table 2) are scattered along the fault planes and joints located at the edges of v1 displaced segments. In the case of sample A7 (Fig. 3C), patches of calcium/silicate composite veins are observable rather than proper veins. This sample matrix is mainly composed of silica (>60%SiO_2,Table 3) and the composition of the patches highly varies from calcium carbonate (>90% CaO, Table 3) to silica (>90% SiO_2,Table 3).

The primary calcium carbonate minerals (Fig. 4) are elongated to fan-shaped and highly damaged with cataclasite and dissolution features. For instance, the calcites of mineralisation stage v1 of sample A5 are fractured perpendicularly to the mineral growth direction and v2 finer mineralisation grew in the interstices (Fig. 4A). Stylolite features are commonly observed in sample A1 veins (Fig. 4B, C), indicating episodes of pressure dissolution. The shape of the primary minerals v1 of A1 can be identified as mainly fan-shaped (Fig. 4B, C, D) with millimetre lengths. Those calcium carbonate minerals are highly damaged, striated or fractured, and embedded in v2 mineralisation (Fig. 4B, E).

The locations of A, B (top) and D (bottom centre) are given on Fig. 3 and are close-ups of areas on samples A5 [U1498B 8R 1W(10 to 12 cm)] and A1 [U1498B 21R 2W(6 to 10 cm)], the vein names v1 to v3 are also indicated on Fig. 3. Some of the primary calcium carbonate minerals are outlined in dashed black on 4B to E. The chemical compositions are electron microprobe analysed.

4.2. Rare Earth elements

The entire Rare Earth Element (REE) dataset measured on each sample was processed with the Mathematical computing software Matlab® developed by MathWorks as to extract a dominant trend per sample. The majority of the measured sampling spots shows a similar trend with few curves scattered up to a few orders of magnitude away from the main data package (A1 example, Fig. 5A). Sample A4 (Fig. 5B), sampled in cherty limestone material as sample A1, shows a differential REE trend from the main calcium carbonate veins (A404) to the silica secondary precipitations (A403) with a slight enrichment in the first LREEs, with a Ce anomaly and a two order of magnitude decrease in the 8 HREEs.

The upper continental crust (UCC-)-normalized REE pattern of this study's carbonate veins vary strongly. The patterns show a main hydrothermal and/or seawater signature; with a minor influence from the serpentine mud (Fig. 6). The 6 LREEs of both A1 and A7 match the Pacific deep-water pattern with REEs low abundance and pronounced negative Ce but without Eu anomalies. Sample A7's HREEs then remarkably well fit the hydrothermal fluids curve whereas sample A1's HREEs fall between those of seawater and hydrothermal fluids, except for a strong enrichment in Lu which is common in all studied carbonates. D5 REE tendency slightly correlates with the hydrothermal fluid curve, with a deeply attenuated Eu positive anomaly (~two orders of magnitude lower). A5 shows the lowest REE values of this study dataset.

The purple, dark blue, light blue and green curves respectively show the REE distributions of the Mariana Trench (Liyan et al., 2003), Pacific deep water (×106 for seawater) (Alibo and Nozaki, 1999), hydrothermal fluids (×106 for fluids) (Douville et al., 2002), and serpentine mud (Kodolányi et al., 2011). The data are UCC normalized based on Taylor and McLennan (1985, 1995) (after Jiang et al., 2018). (For interpretation of the references to color in this figure legend, the reader is referred to the web version of this article.)

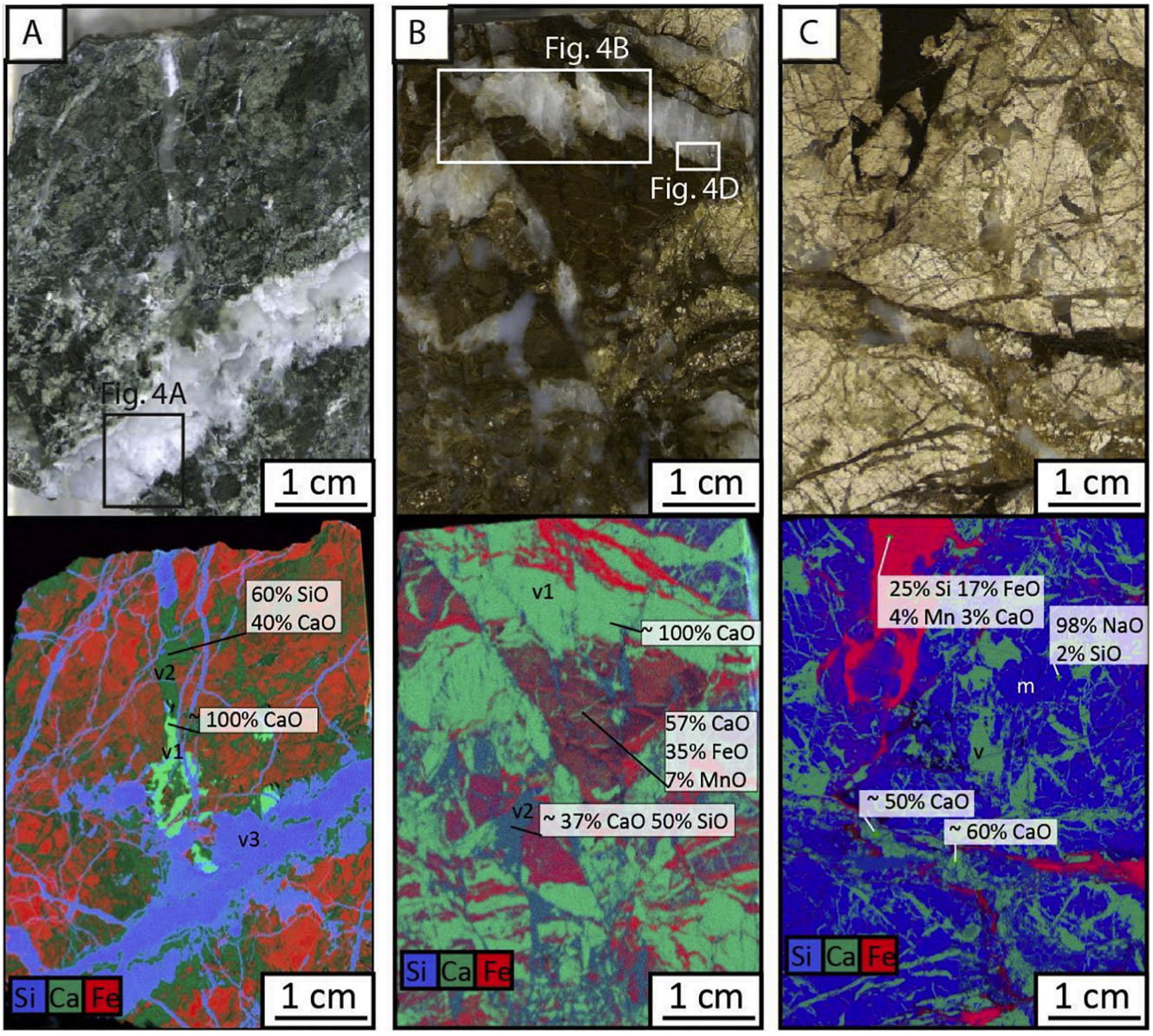

Fig. 3. Macroscopic petrology (top) and microbeam X-Ray Fluorescence (XRF) (Bruker M4 TORNADO TM) imaging (bottom) of the vein network of samples (A) U1498B 8R 1 W(10 to 12 cm), (B) U1498B 21R 2 W(6 to 10 cm), (C) U1498B 21R 2 W(26 to 29 cm). In this study those IODP samples are respectively recalled A5, A1 and A7. v stands for vein and m for matrix.

Table 1
Electron microprobe analyses of the veins, sample A5 [U1498B 183 8R 1 W (10 to 12 cm)].

Analysis	A5-1-1	A5-1-2	A5-1-2	A5-2-3	A5-3-1
Location	v3	v2	v2	v1	v1
Composition in norm. wt% of oxides					
Na2O	9.3	0.9	9.7		
SiO2	53.8	15.0	54.9	14.0	12.6
CaO	35.0	60.0	33.6	56.3	59.1
Cr2O3	0.9				
Al2O3		6.6		7.3	7.0
SO3		17.5	1.3	22.4	21.3
MnO					
FeO					
Total	99.0	100.0	99.5	100.0	100.0

*v stands for “vein” and m for “matrix”.

Table 2
Electron microprobe analyses of the veins, sample A1 [U1498B 21R 2 W (6 to 10 cm)].

Analysis	A1-2-5	A1-2-9	A1-3-4	A1-3-5
Location	v1	v1	v2	v2
Composition in norm. wt% of oxides				
Na2O			8.0	9.0
SiO2	3.2	1.3	53.1	51.7
CaO	95.7	98.6	37.9	38.4
Cr2O3				
Al2O3				
SO3				
MnO			1.0	1.0
FeO				
Total	98.9	100.0	100.0	100.0

*v stands for “vein” and m for “matrix”

Table 3
Electron microprobe analyses of the veins, sample A7 [U1498B 21R 2 W (26 to 29 cm)].

Analysis	A7-1	A7-2	A7-2-3	A7-2-4	A7-1-11
Location	v	v	m	m	v
Composition in norm. wt% of oxides					
Na2O	12.1	11.1		8.0	0.91075
SiO2	51.5	51.7	93.9	65.2	6.45033
CaO	32.9	27.1		7.3	92.6389
Cr2O3	1.1	0.9			
Al2O3					
SO3					
MnO	2.4	7.7		5.8	
FeO			1.5	13.7	
Total	100.0	98.5	95.4	100.0	100.0

*v stands for "vein" and m for "matrix".

4.3. Srontium, carbon and oxygen isotopes

The $^{87}Sr/^{86}Sr$ ratios fit the narrow range 0.704977 (+/− 7*-10^{-6}) to 0.705798 (+/−−10^{-6}) (Table 4). Those values (Fig. 7) lie closer to the Mariana extrusive volcanic and Paleogene tuffs than the Pacific plate sediment $^{87}Sr/^{86}Sr$ values measured during previous ocean drilling expeditions (DSDP leg 6, Leg 20 and ODP Leg 199; Ito and Stern, 1986) and the mean seawater trends (Spooner et al., 1977; Veizer et al., 1999). However, $\delta^{18}O$ ranging from 18.7 to 19.8 (V-SMOW) ‰ (Table 4) fit better with the seawater and sediment $\delta^{18}O$ signatures.

DSP Leg 20 and ODP Legs 198/199 drill Sites are located on the subducted Pacific Plate and targeted the subducted sedimentary pile, see Ito and Stern (1986) for additional details.

4.4. U-Pb datings

U-Pb absolute dating of the calcium carbonate veins of samples A1, A7 and D5 (Fig. 8) indicate Late Eocene to Quaternary precipitation of the calcium carbonate veins, respectively 8.2 (±3.4), 19 (±21) and 25 (±11) My. The uncertainty on those dates is high, due to the huge amount of common Pb. Sample A1 carbonate veins are the youngest with a post Tortonian age, whereas sample D5 veins are the oldest, Bartonian to Serravallian. Given the uncertainty on sample A7's laser-ablation U-Pb dating, this sample's veins precipitation can only be restricted to late Eocene to present day.

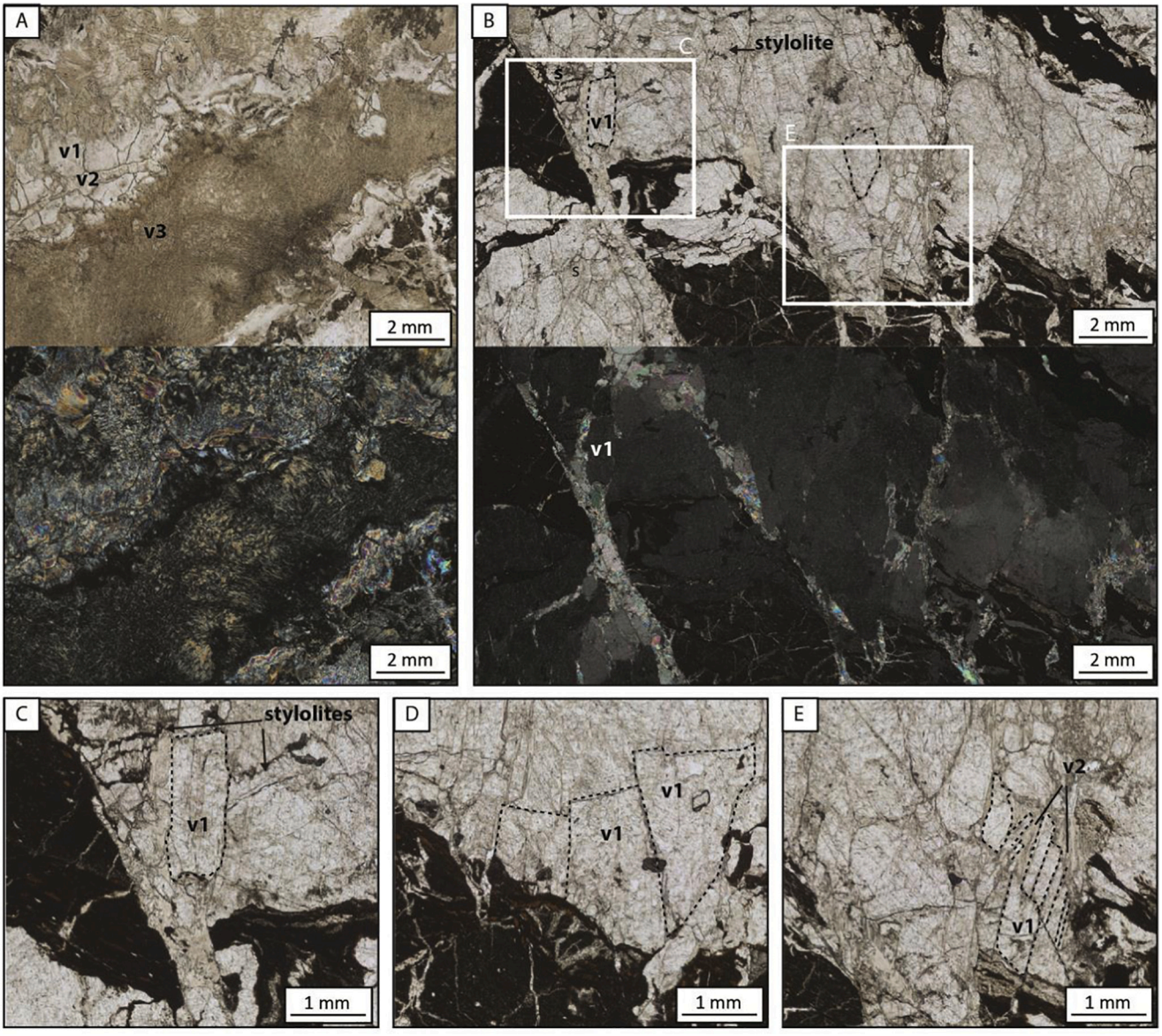

Fig. 4. Optical evidence of primary mineral growth, dissolution and structural features in carbonate veins.

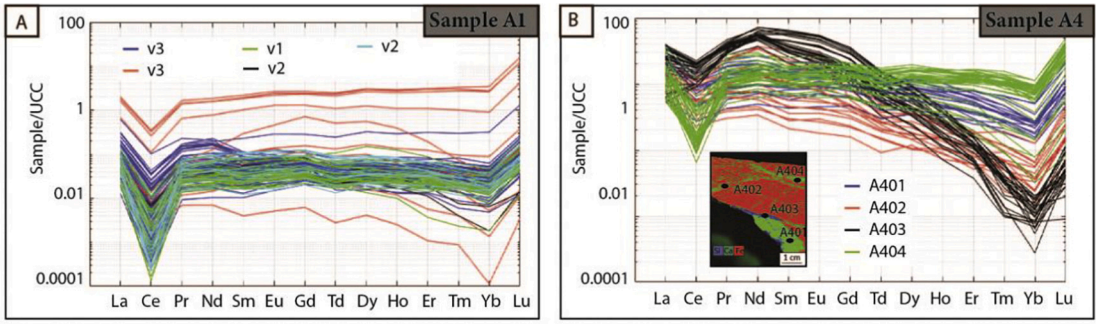

Fig. 5. Examples of UCC-normalized REE patterns of each sampling point in the case of (A.) sample A1 data extracted in the veins v1, v2 and v3 localized Fig. 3 and (B.) sample A4 [366-U1498B-21R-2-W (26 to 29-cm)] with sampling point located on an X-Ray Fluorescence (XRF) image compiling Si, Ca and Fe elements, the veins are composed of Si and Ca. The first light six elements (La, Ce, Pr, Nd, Sm and EU) are called LREEs in this article and the 8 heavy elements (*Gd, Tb,* Dy, Ho, Er, Tm, Yb, and Lu).are called HREEs. Ample A4 too low uranium contant to be dated.

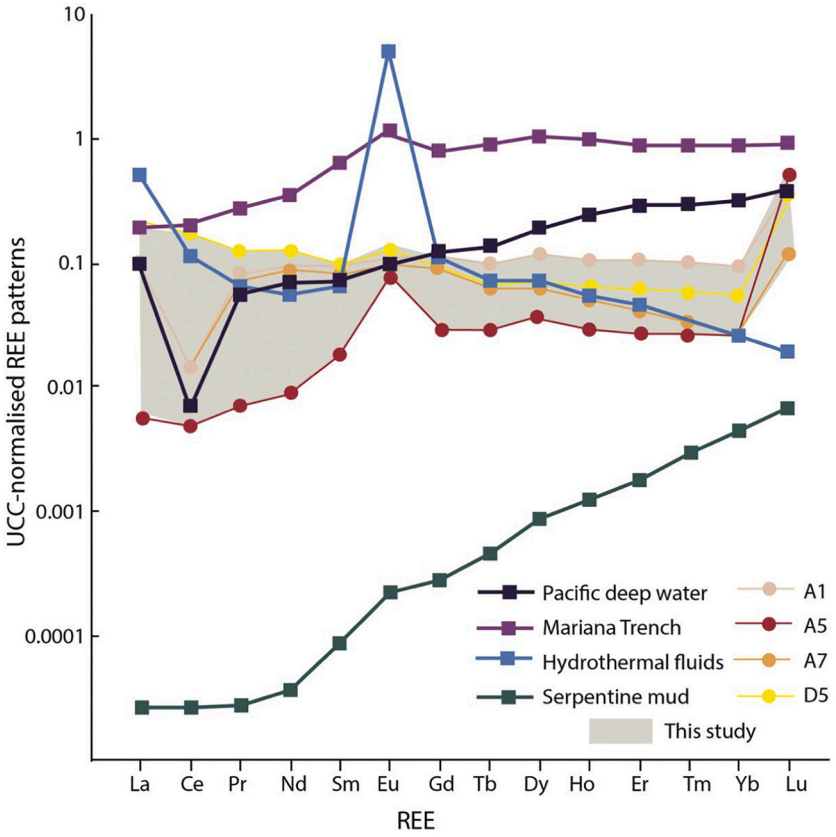

Fig. 6. UCC-normalized REE patterns of this study carbonate veins samples, serpentine mud, present-day marine sediments and seawater.

The carbonate veins of sample A5 precipitated 82 (±38) My ago. These veins have hence formed during Early Cretaceous (120 My) to Late Cretaceous (44 My) times. This sample contains by far the oldest of the here-investigated carbonates, even when considering the large uncertainties of these ages.

5. Discussion

5.1. Chronology of the Pacific plate sediments subduction and mud volcanoes building up

We here discuss an episodic formation of the Mariana mud volcanoes from subduction initiation to present day (Fig. 9). Mariana convergence started ~50 My ago (Fryer et al., 1990; Mrozowski and Hayes, 1980), and numerous extensional faults accommodated the primary forearc spreading (Stern, 2004), which initiated pathways for slab-derived fluids and materials of the subducting plate as well as of the supra-subduction mantle to rise from the subduction channel mélange zone to the seafloor (Wheat et al., 2020), where the mud volcanoes formed (Fig. 9A).

The ages of this study's carbonate veins range from Early Cretaceous to present day (Fig. 8) and have recorded fluid circulation in potentially four different extensional systems respectively a) pre-subduction, on a plate seamount before it was subducted b) in the Mélange zone, pre-exhumation, c) within the forearc fault system, or d) within a mud volcano edifice.

The samples A1, A7 and D5 late Eocene to Quaternary ages are contemporaneous with the mud volcanism and could be related to either

Table 4
$^{87}Sr/^{86}Sr$, $\delta^{13}C$ (‰, V-PDB) and $\delta^{18}O$ (‰, V-SMOW) stable isotope analyses of this study carbonate veins.

Sample	Reference	$^{87}Sr/^{86}Sr$	±2σ	$\delta^{13}C$ (‰V-PDB)	±2σ	$\delta^{18}O$ (‰ V-SMOW)	±2σ
A1	U1498B 21R 2 W (6 to 10 cm)	0.705350	4.8E-06	2.0	1E-01	19.1	2E-01
A4	U1498B 21R 2 W (26 to 29 cm)	0.705252	5.1E-06	n.m.	n.m.	n.m.	n.m.
A5	U1498B 8R 1 W (10 to 12 cm)	0.705144	1.4E-05	1.0	1E-01	19.8	2E-01
A7	U1498B 21R 2 W (26 to 29 cm)	0.705347	6.2E-06	2.0	1E-01	19.5	2E-01
B11	U1497B 27F1 2 W (43 to 47 cm)	0.705114	7.3E-06	3.1	1E-01	19.5	2E-01
D4	U1496A 1F 2 W (31 to 32 cm)	0.704977	7.0E-06	n.m.	n.m.	n.m.	n.m.
D5	U1498A 3R 2 W (0 to 3 cm)	0.705798	6.8E-06	2.2	1E-01	18.7	2E-01

n.m. stands for "not measured".

the exhumation process through the forearc normal fault system or precipitation processes within the mud volcano structure (Fig. 9). Shearing and cataclastic structures and stylolites observed on-board and in A1, A5, and A7 cases (Fig. 2, Fig. 4, Fryer et al., 2018) show that the samples underwent high tectonic stress and pressure conditions.

Sample A5 U-Pb ages, ranging from Early Cretaceous (120 My) to Lutetian (41.2 My) cannot support a specific tectonic event directly linkable with the carbonate veins precipitation. However, those veins clearly precipitated before or during the early stages of exhumation. Many extension stages could have affected these rocks before the exhumation (Fig. 9), from the initial setting up on a volcanic island or a seamount to the slab faulting in the flexural zone (Funnell et al., 2017) or the edifice deformation upon subduction. The vein system affecting the metabasite is dense and well localized within this domain (Fig. 2B). Even the cherty limestone in primary contact with the metabasalts did not show the same deformation and vein formation (Fig. 2C), which supports localized deformation and hydrothermal fluid flow.

5.2. Precipitation mechanisms

The extensional fault system accommodating uplift of the forearc ridge upon which Fantangisña Seamount formed is complex and should imply fault linkage and relay (e.g., Fossen and Rotevatn, 2016), offering many potential pathways for the fluid and mud circulation through or along the fault segments (Fig. 9), depending on the modifications of the fault permeability by triggers such as mud overpressures or earthquakes (Gratier, 2011). As shown by field observations in extensional systems, the highest amount of fluid circulation in a fault system tends to be localized in fault relays, where displacement is transferred across linking structures between two fault segments (Gartrell et al., 2003; Micarelli et al., 2006; Frery et al., 2017).

Serpentine mudflows were at least recorded from Neogene until present day, as attested by, among other indications, Miocene or Pliocene nanofossils sampled in the first hundreds meters cored on Fantangisña seamount flank (U1498A, Fryer et al., 2017), Upper Miocene to Upper Pleistocene serpentine mudflow layers interbedded with sediments on Asùt Tesoru seamount (Kurz et al., 2017) and active serpentinite mudflow and slab-fluid seeps observed at the summit of some of the Mariana forearc mud volcanoes (Fryer et al., 1999, 2006). The episodicity of those events is demonstrated on the flank of Conical Seamount, located about 80 km west of the Mariana Trench axis. Six units composed of serpentine mud flows were recorded from 300 m of

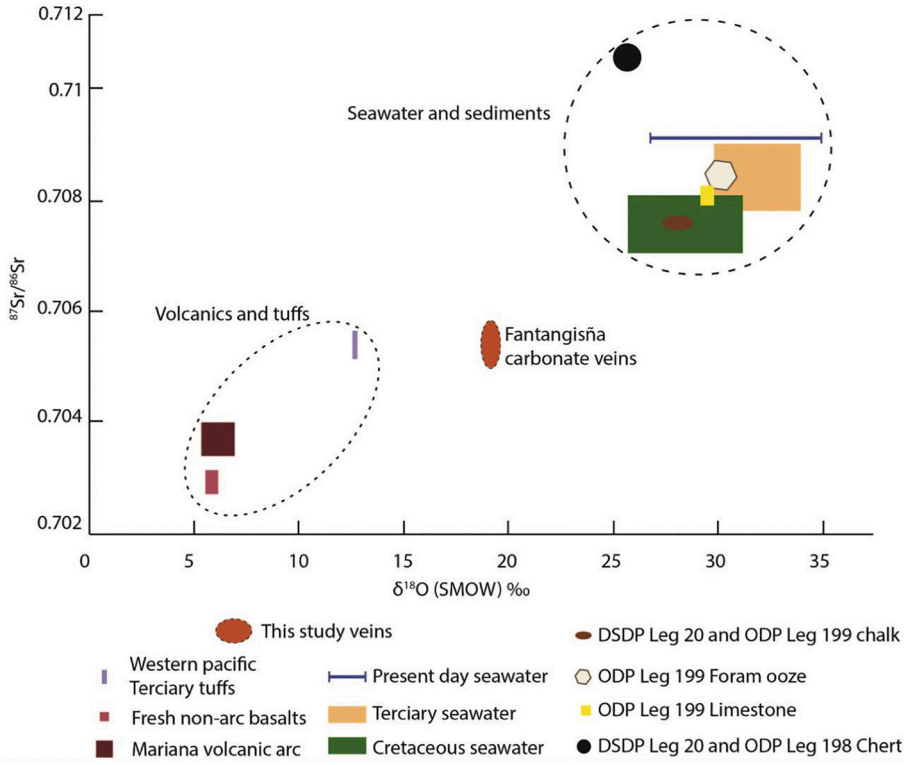

Fig. 7. $^{87}Sr/^{86}Sr$ ratios vs. function of $\delta^{18}O$ signatures.

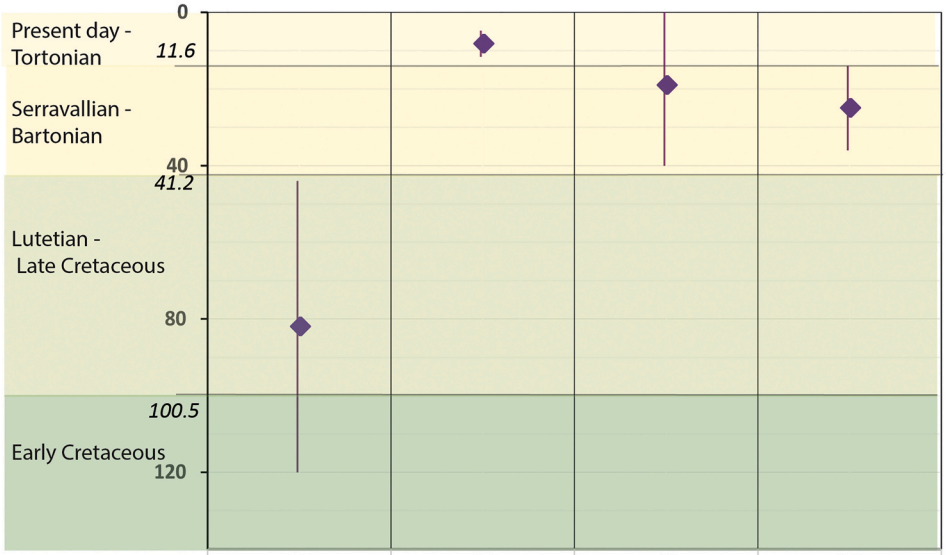

	A5	A1	A7	D5
◆ U-Pb dating (My)	82	8.2	19	25
High (My)	120	11.6	40	36
Low (My)	44	4.8	-2	14
	U1498B 8R 1 W (10 to 12 cm)	U1498B 21R 2W (6 to 10 cm)	U1498B 21R 2W (26 to 29 cm)	U1498A 3R 2W (0 to 3 cm)

Fig. 8. U-Pb absolute dating by laser-ablation for four selected samples.

drilling (hole 779A, LEG 125, Fryer and Mottl, 1992). Each unit is composed of a sequence of pulses ranging from a few tens of meters to a few centimetres, indicating variable volumes and rates of episodic serpentine mudflow events from Lower Pliocene to Holocene (Fryer et al., 1989). Those serpentine mudflows are likely to be related to the activity of at least two major faults intersecting below Conical Seamount (Fryer et al., 1992). Pelagic sediments capping the mudflows (Fryer et al., 1989) seem to indicate periods with no mud volcanism activity and can be related to a decrease in inter-seismic fault permeability by gouge compaction and fracture healing and sealing (Renard et al., 2000; Gratier et al., 2009; Gratier, 2011). However, the duration of those periods is difficult to evaluate given the thinness of the pelagic layers.

5.3. *Origin of the fluid and potential trigger event*

The Marianna mud volcanos are dynamic and erupt episodically. In this study, we observed episodes of fluid circulation/precipitation in open fractures from Late Cretaceous to ~8.2 My (±3.4My). Those circulation events are now embedded in the mud and (i) can be or (ii) not be related to the mud volcanism. Several events of mud volcanism have been identified in the literature from Eocene to present day. The upper serpentinite mud layers cored on the flank of Fantangisña seamount lay above pelagic sediments that are upper Miocene, dating the most recent mud volcanism events recorded in this seamount in the range of 10 My (Menapace et al., 2019). Other holes showed that Asut Tesoru Seamount may have been active since the Eocene, based on analysis of two serpentine-bearing (~50% serpentine) sediment intervals immediately above Eocene basement recovered during Deep Sea Drilling Project (DSDP) Leg 60 at Site 459 (Desprairies, 1982; Fryer et al., 2017). Those events have been observed in the shallowest mud layers of the mud volcanoes that the ocean drilling program was able to drill and, considering the thickness of the mud volcano, it is highly probable that the mud volcanism started early in the subduction process.

The muds in a given eruptive state may reflect a complicated mixture of materials from the deep subduction channel plus the addition of materials emplaced in the shallower conduit region during previous eruptions. Differences in Sr isotopic signatures from this study samples permit the distinction from the different sources. The results show that sample A5 has relative less radiogenic strontium ratio comparing to the other samples' IODP references (A1, A7 and D5 – Table 4). This less radiogenic Sr value can reflect a greater proportion of contribution from the mantle components. According to the literature (Pearce et al., 1995; Han et al., 1997) mantle components are depleted in Sr during the fractional crystallization of the magma. This suggestion corroborates the carbonate precipitation at greater depth, before/ during the exhumation.

The sub-parallel elongated minerals (Fig. 4) could indicate crystallization under stress (e.g., Bons and Montenari, 2005; Gratier et al., 2012). The fan-shaped calcium carbonate minerals could indicate the precipitation of a free fluid in an open fracture, either resulting from a primary circulation event or previous dissolution episodes (Billi et al., 2007), as supported by the occurrence of both mineralisation types within an individual displaced vein and the occurrence of stylolite features (Fig. 4). However, sample D5 is coming from drill hole 1498A whereas the other samples are from the hole 1498B. The current pore fluids' PH as well as the Mg and silica contents differ between those two holes (Fryer et al., 2018) and can potentially influence the type and rate of carbonate precipitation.

The progressive silicification of the carbonate veins (Fig. 3) could indicate a low-temperature, structure-controlled event (Auclair et al., 1993; Kbulut et al., 2006) as well as a change in pH, a variation in composition of the same fluid due to fluid/wall rock interaction or to two separate fluid influxes (Uçurum et al., 1996; Uçurum, 2000).

The UCC-normalized LREEs pattern (Fig. 6), $^{87}Sr/^{86}Sr$ ratios ranging from 0.704977 to 0.705798 (Table 4) and $\delta^{18}O$ values of 18.7 to 19.8 (‰, V-SMOW) (Fig. 7) of this study's carbonate veins indicate a mixed origin of the precipitated fluids, influenced by interaction with the surrounding serpentinite mudflow material, as the $^{87}Sr/^{86}Sr$ values inthe pore fluids ranges from 0.70495 to 0.70585 at Fantangisña, seamount and from 0.70523 to 0.70538 in Metavolcanic material (Albers et al., 2019; Fig. 7). The veins could have recorded several precipitation stages, from fluids with a mantle signature at the slab

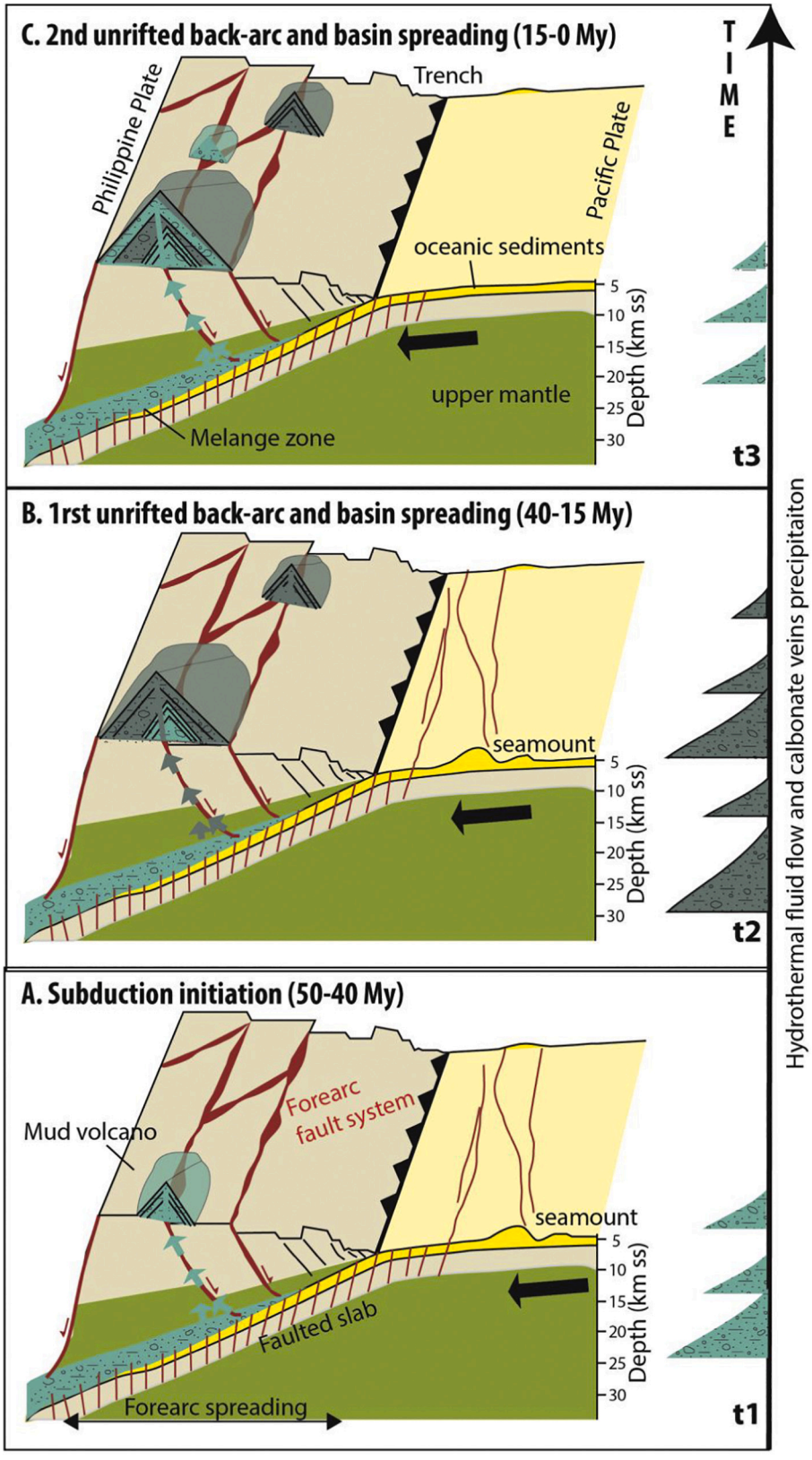

Fig. 9. Spatio-temporal model of episodic fluid circulation and precipitation from the subduction zone up to the mud volcanoes A. Subduction initiation (50–40 My); B. 1rst unrifted back-arc and basin spreading (40–15 My); C. 2nd unrifted back-and basin spreading (15-0My).

depth to a mix of shallow hydrothermal fluids and seawater close to the seafloor within the mud volcano. The UCC-normalized LREE pattern and the high degree of silicification of the oldest veins (A5, Fig. 8) are comparable with other studies (Albers et al., 2019) and support the hypotheses of an early precipitation during the convergence processes followed by diagenetic processes during the exhumation and contact with the serpentinite mud, within the subduction channel mélange zone and/or within the mud volcano edifice. Considering a mean carbonate $\delta^{18}O$ signature of 19‰, V-SMOW) and Fantangisña seamount water's $\delta^{18}O$ signature of 0‰, V-SMOW (Debret et al., 2019), we can compute from Epstein et al. (1953) a mean precipitation temperature of 100.7 °C supporting an early diagenesis process. Debret et al., 2019 discuss the serpentinization process and estimate a mean formation temperature of the "blue serpentine" minerals of 183 °C. Albers et al., 2019 calculated estimated temperatures of carbonate formation below 100 °C and shifted those value to 130 to 175 °C and 220 to 310 °C as to account for the conditions of precipitation at depth, below the mud volcanoes, that are inferred to be the location of formation of the carbonate veins.

The early stage of silicification of the younger veins (A1,Fig. 8) and the partial match between UCC-normalized LREE pattern (only the LREE 6 elements, Fig. 8) and the Pacific deep water profile could indicate a short residence time in shallow conditions, within the mud volcano edifice. Those veins are cataclastically deformed, previously interpreted as a record of the early exhumation stages within the normal fault system deeply rooted in the subduction channel mélange zone (Fryer et al., 2018). However, the UCC-normalized HREEs pattern and the $^{87}Sr/^{86}Sr$ ratios still support a precipitation at greater depth, before/ during the exhumation. Modelling studies showed that the Mariana mud volcanoes spread laterally from a central conduit (Oakley et al., 2008). Those observations tend to support the opening of potential secondary faults within the mud volcanoes that can directly drive the uprising material to the flanks of the volcanoes (Fig. 9). The carbonate vein ages spread over tens of million years (Fig. 8) supporting the existence of episodic serpentine mud eruptions from depth up to the subsurface or up to the surface of the mud volcanoes. The main conduit can be obstructed during non-activity periods and secondary circulation pathways could be triggered by overpressure, as recorded in travertine structures (Frery et al., 2015), or a normal faulting event at the base of the volcano, opening a high-angle pathway toward the edifice or an upturning fault toward the flank of the edifice as modelled in the case of stratovolcanoes (Vidal and Merle, 2000).

6. Conclusions

Serpentinite mud volcanoes' carbonate veins can be dated with U-Pb absolute dating by laser-ablation, providing a history of fluid precipitation in a brittle system from at least the early exhumation stages to edifice building.

We propose a rapid exhumation process and formation of the youngest carbonate veins on the flank of the mud volcanoes. Those edifices are episodically active during development of the forearc fault system. This is expressed by a complex fault system preserved within the edifice, with secondary flank faults (such as those indicated on the west side of Fantangisña Seamount) potentially used by the uprising serpentinite mud instead of or simultaneously with the central conduit.

Declaration of Competing Interest

None.

Data availability

Cyclicity of structural flow in an active subduction system, new insights from mud volcano's carbonate veins – Scientific ocean drilling expedition IODP 366- dataset (Original data) (CSIRO Research Publications Repository)

Acknowledgments

We acknowledge funding from IODP and the Australian IODP Office - our results depend on IODP's scientific ocean drilling and Australian/NZ support of this program and the Austrian Science Fund (FWF-P 31683-N29). The authors also would like to thank Dr. Susanne Schmid and Michael Verrall from CSIRO for their advises and help on the petrological analyses.

References

Albers, E., Bach, W., Klein, F., Menzies, C.D., Lucassen, F., Teagle, D.A., 2019. Fluid–rock interactions in the shallow Mariana forearc: carbon cycling and redox conditions. Solid Earth 10 (3), 907–930.
Alibo, D.S., Nozaki, Y., 1999. Rare earth elements in seawater: particle association, shale-normalization, and Ce oxidation. Geochim. Cosmochim. Acta 63 (3–4), 363–372.
Auclair, M., Gauthier, M., Trottier, J., Jebrak, M., Chartrand, J., 1993. Mineralogy, geochemistry, and paragenesis of the Eastern metals serpentinite-associated Ni-Cu-Zn deposit, Quebec Appalachians. Econ. Geol. 88 (1), 123–138.
Beaudoin, N., Lacombe, O., Roberts, N.M.W., Koehn, D., 2018. U-Pb dating of calcite veins reveals complex stress evolution and thrust sequence in the Bighorn Basin, Wyoming, USA. Geology 46 (11), 1015–1018.
Billi, A., Valle, A., Brilli, M., Faccenna, C., Funiciello, R., 2007. Fracture-controlled fluid circulation and dissolutional weathering in sinkhole-prone carbonate rocks from Central Italy. J. Struct. Geol. 29 (3), 385–395.
Bons, P.D., Montenari, M., 2005. The formation of antitaxial calcite veins with well-developed fibres, Oppaminda Creek, South Australia. J. Struct. Geol. 27 (2), 231–248.
Byerlee, J., 1990. Friction, overpressure and fault normal compression. Geophys. Res. Lett. 17 (12), 2109–2112.
Childs, C., Sylta, Ø., Moriya, S., Morewood, N., Manzocchi, T., Walsh, J.J., Hermanssen, D., 2009. Calibrating fault seal using a hydrocarbon migration model of the Oseberg Syd Area, Viking Graben. Mar. Pet. Geol. 26 (6), 764–774.
Coplen, T.B., 1995. Discontinuance of SMOW and PDB. Nature 375 (6529), 285.
Debret, B., Albers, E., Walter, B., Price, R., Barnes, J.D., Beunon, H., Facq, S., Gillikin, D. P., Mattielli, N., Williams, H., 2019. Shallow forearc mantle dynamics and geochemistry: new insights from IODP Expedition 366. Lithos 326, 230–245.
Desprairies, A., 1982. Authigenic minerals in volcanogenic sediments cored during Deep Sea Drilling Project Leg 60. In: Hussong, D.M., Uyeda, S., et al. (Eds.), Initial Reports of the Deep Sea Drilling Project, 60. U.S. Government Printing Office, Washington, DC, pp. 455–466. https://doi.org/10.2973/dsdp.proc.60.120.1982.
Dockrill, B., Shipton, Z.K., 2010. Structural controls on leakage from a natural CO2 geologic storage site: Central Utah, USA. J. Struct. Geol. 32 (11), 1768–1782.
Douville, E., Charlou, J.L., Oelkers, E.H., Bienvenu, P., Jove Colon, C.F., Donval, J.P., Fouquet, Y., Prieur, D., Appriou, P., 2002. The Rainbow Vent Fluids (36 14′ N, MAR): the Influence of Ultramafic Rocks and phase Separation on Trace Metal Content in Mid-Atlantic Ridge Hydrothermal Fluids. Chem. Geol. 184 (1–2), 37–48.
Epstein, E., Samuel, W., et al., 1953. Revised carbonate-water isotopic temperature scale. Geol. Soc. Am. Bull. 64 (11), 1315–1326.
Faulkner, D.R., Rutter, E.H., 2001. Can the maintenance of overpressured fluids in large strike-slip fault zones explain their apparent weakness? Geology 29 (6), 503–506.
Fossen, H., Rotevatn, A., 2016. Fault linkage and relay structures in extensional settings—A review. Earth Sci. Rev. 154, 14–28.
Frery, E., Gratier, J.P., Ellouz-Zimmerman, N., Loiselet, C., Braun, J., Deschamps, P., Blamart, D., Hamelin, B., Swennen, R., 2015. Evolution of fault permeability during episodic fluid circulation: evidence for the effects of fluid–rock interactions from Travertine Studies (Utah–USA). Tectonophysics 651, 121–137.
Frery, E., Gratier, J.P., Ellouz-Zimmerman, N., Deschamps, P., Blamart, D., Hamelin, B., Swennen, R., 2017. Geochemical Transect through a Travertine Mount: A Detailed Record of CO2-Enriched Fluid Leakage from Late Pleistocene to Present-Day–Little Grand Wash Fault (Utah, USA). Quat. Int. 437, 98–106.
Fryer, P., Mottl, M.J., 1992. Lithology, mineralogy, and origin of serpentine muds recovered from conical and torishima forearc seamounts: results of Leg 125 Drilling. In: Fryer, P., Pearce, J.A., Stokking, L.B., et al. (Eds.), Proc. ODP, Sci. Results. Ocean Drilling Program, College Station, TX, pp. 343–362. https://doi.org/10.2973/odp.proc.sr.125.126.1992.
Fryer, P., Salisbury, M.H., 2006. Leg 195 Synthesis: Site 1200-Serpentinite Seamounts of the Izu-Bonin/Mariana Convergent Plate Margin (ODP Leg 125 and 195 Drilling Results). In: Proc. ODP, Sci. Results, 195, pp. 1–30.
Fryer, P., Pearce, J.A., ODP Leg and Shipboard Party, 1989. ODP Leg 125 Drills Forearc Crust, Mantle. Geotimes 34 (7), 18–20.
Fryer, P., Saboda, K.L., Johnson, L.E., Mackay, M.E., Moore, G.F., Stoffers, P., 1990. Conical Seamount: SeaMARC II, Alvin Submersible, and Seismic Reflection Studies. In: Proc. Ocean Drill. Program Sci. Results, 125, pp. 3–11.
Fryer, P., Pearce, J.A., Stokking, L.B., 1992. A Synthesis of Leg 125 Drilling of Serpentine Seamounts on the Mariana and Izu–Bonin Forearcs. In: Proceedings of the Ocean Drilling Program, 125. Scientific Results, pp. 593–614.
Fryer, P., Wheat, C.G., Mottl, M.J., 1999. Mariana Blueschist Mud Volcanism: Implications for Conditions within the Subduction Zone. Geology 27 (2), 103–106.
Fryer, P., Gharib, J., Ross, K., Savov, I., Mottl, M.J., 2006. Variability in serpentinite mudflow mechanisms and sources: ODP drilling results on Mariana Forearc Seamounts. Geochem. Geophys. Geosyst. 7 (8).

Fryer, P., Wheat, G., Williams, T., the Expedition 366 Scientists, 2017. Expedition 366 Preliminary Report: Mariana Convergent Margin and South Chamorro Seamount. International Ocean Discovery Program. https://doi.org/10.14379/iodp.pr.366.2017.

Fryer, P., Wheat, C.G., Williams, T., the Expedition 366 Scientists, . Proceedings of the International Ocean Discovery Program Volume 366. publications.iodp.org. https://doi.org/10.14379/iodp.proc.366supp.2018.

Fryer, P., Wheat, C.G., Williams, T., Kelley, C., Johnson, K., Ryan, J., Debret, B., 2020. Mariana serpentinite mud volcanism exhumes subducted seamount materials: implications for the origin of life. Philosophical Transactions of the Royal Society A 378 (2165), 20180425.

Funnell, M.J., Peirce, C., Robinson, A.H., 2017. Structural variability of the Tonga-Kermadec Forearc characterized using robustly constrained geophysical data. Geophys. J. Int. 210 (3), 1681–1702.

Gartrell, A., Zhang, Y., Lisk, M., Dewhurst, D., 2003. Enhanced hydrocarbon leakage at fault intersections: an example from the Timor Sea, Northwest Shelf, Australia. J. Geochem. Explor. 78, 361–365.

Gratier, J.P., 2011. Fault Permeability and Strength Evolution Related to Fracturing and Healing Episodic Processes (Years to Millennia): the Role of Pressure Solution. Oil & Gas Science and Technology–Revue d'IFP Energies Nouvelles 66 (3), 491–506.

Gratier, J.P., Favreau, P., Renard, F., Pili, E., 2002. Fluid pressure Evolution during the Earthquake Cycle Controlled by Fluid Flow and pressure solution Crack Sealing. Earth Planets Space 54 (11), 1139–1146.

Gratier, J.P., Guiguet, R., Renard, F., Jenatton, L., Bernard, D., 2009. A pressure solution Creep Law for Quartz from Indentation experiments. J. Geophys. Res. 114 (B3).

Gratier, J.P., Frery, E., Deschamps, P., Røyne, A., Renard, F., Dysthe, D., Ellouz-Zimmerman, N., Hamelin, B., 2012. How Travertine Veins Grow from top to Bottom and lift the Rocks above Them: the effect of Crystallization Force. Geology 40 (11), 1015–1018.

Han, B.F., Wang, S.G., Jahn, B.M., Hong, D.W., Kagami, H., Sun, Y.L., 1997. Depleted-mantle source for the Ulungur River A-type granites from North Xinjiang, China: geochemistry and Nd–Sr isotopic evidence, and implications for Phanerozoic crustal growth. Chem. Geol. 138 (3–4), 135–159.

Hansman, R.J., Albert, R., Gerdes, A., Ring, U., 2018. Absolute Ages of Multiple Generations of Brittle Structures by U-Pb Dating of Calcite. Geology 46 (3), 207–210.

Ito, E., Stern, R.J., 1986. Oxygen-and Strontium-Isotopic Investigations of Subduction Zone Volcanism: the Case of the Volcano Arc and the Marianas Island Arc. Earth Planet. Sci. Lett. 76 (3–4), 312–320.

Jiang, Z., Sun, Z., Liu, Z., Cao, H., Geng, W., Xu, H., Wang, L., 2018. Rare-Earth Element Geochemistry reveals the Provenance of Sediments on the Southwestern margin of the Challenger deep. J. Oceanol. Limnol. 1–12.

Kbulut, M., Pišk̈in, O., & Karayiğ̈it, A.I, 2006. The Genesis of the Carbonatized and Silicified Ultramafics Known as Listvenites: A Case Study from the Mihalıççık Region (Eskişehir), NW Turkey. Geol. J. 41 (5), 557–580.

Kodolányi, J., Pettke, T., Spandler, C., Kamber, B.S., Gméling, K., 2011. Geochemistry of Ocean Floor and Fore-Arc Serpentinites: Constraints on the Ultramafic Input to Subduction zones. J. Petrol. 53 (2), 235–270.

Kurz, W., Micheuz, P., Grunert, P., Auer, G., Reuter, M., 2017. Seamount Subduction and Serpentinite Mud Volcanisms in the Mariana Convergent Margin System: Time Constraints from Micropaleontological Studies (IODP Expedition 366) (In AGU Fall Meeting Abstracts).

Liyan, T., Guangtao, Z., Zuolin, C., 2003. The preliminary Study of Petrological Geochemistry of Basalts from Hydrothermal activity Regions, Mariana Trough. J. Univ. Qingdao, Chinese edition 33 (3), 405–412.

Menapace, W., Tangunan, D., Maas, M., Williams, T., Kopf, A., 2019. Rheology and biostratigraphy of the Mariana serpentine muds unravel mud volcano evolution. J. Geophys. Res. 124 (11), 10752–10776.

Micarelli, L., Moretti, I., Jaubert, M., Moulouel, H., 2006. Fracture Analysis in the South-Western Corinth Rift (Greece) and Implications on Fault Hydraulic Behavior. Tectonophysics 426 (1–2), 31–59.

Mrozowski, C.L., Hayes, D.E., 1980. A Seismic Reflection Study of Faulting in the Mariana Fore Arc. In: The Tectonic and Geologic Evolution of Southeast Asian Seas and Islands, pp. 223–234.

Nuriel, P., Weinberger, R., Kylander-Clark, A.R.C., Hacker, B.R., Craddock, J.P., 2017. The Onset of the Dead Sea Transform based on Calcite Age-Strain analyses. Geology 45 (7), 587–590.

Oakley, A.J., Taylor, B., Moore, G.F., 2008. Pacific Plate Subduction beneath the Central Mariana and Izu-Bonin Fore Arcs: New Insights from an Old margin. Geochem. Geophys. Geosyst. 9 (6).

Paton, C., Woodhead, J.D., Hellstrom, J.C., Hergt, J.M., Greig, A., Maas, R., 2010. Improved Laser Ablation U-Pb Zircon Geochronology through Robust Downhole Fractionation Correction. Geochem. Geophys. Geosyst. 11 (3).

Pearce, J.A., Baker, P.E., Harvey, P.K., Luff, I.W., 1995. Geochemical evidence for subduction fluxes, mantle melting and fractional crystallization beneath the South Sandwich island arc. J. Petrol. 36 (4), 1073–1109.

Renard, F., Gratier, J.P., Jamtveit, B., 2000. Kinetics of Crack-Sealing, Intergranular pressure solution, and Compaction around active Faults. J. Struct. Geol. 22 (10), 1395–1407.

Rice, J.R., 1992. Fault stress States, Pore pressure Distributions, and the weakness of the San Andreas Fault. Int. Geophys. 51, 475–503. Elsevier.

Ring, U., Gerdes, A., 2016. Kinematics of the Alpenrhein-Bodensee Graben System in the Central Alps: Oligocene/Miocene Transtension due to Formation of the Western Alps Arc. Tectonics 35 (6), 1367–1391. https://doi.org/10.1002/2015TC004085.

Roberts, N.M.W., Walker, R.J., 2016. U-Pb Geochronology of Calcite-Mineralized Faults: absolute timing of Rift-Related Fault events on the Northeast Atlantic margin. Geology 44 (7), 531–534. https://doi.org/10.1130/G37868.1.

Salisbury, M.H., Shinohara, M., Richter, C., Araki, E., Barr, S.R., D'Antonio, M., Dean, S. M., Diekmann, B., Edwards, K.M., Fryer, P., 2002. Leg 195 Summary. Proc. Ocean Drill. Program Initial Rep 22–32.

Sibson, R.H., 1994. Crustal stress, Faulting and Fluid Flow. Geol. Soc. Lond., Spec. Publ. 78 (1), 69–84.

Sleep, N.H., Blanpied, M.L., 1994. Ductile Creep and Compaction: A Mechanism for Transiently increasing Fluid pressure in mostly Sealed Fault zones. Pure Appl. Geophys. 143 (1–3), 9–40.

Spooner, E.T.C., Chapman, H.J., Smewing, J.D., 1977. Strontium isotopic contamination and oxidation during ocean floor hydrothermal metamorphism of the ophiolitic rocks of the Troodos Massif, Cyprus. Geochimica et Cosmochimica Acta 41 (7), 873–890.

Stern, R.J., 2004. Subduction Initiation: Spontaneous and Induced. Earth Planet. Sci. Lett. 226 (3–4), 275–292.

Taylor, S.R., McLennan, S.M., 1985. The Continental Crust: Its Composition and Evolution. Blackwell Scientific Publications, p. 312.

Taylor, S.R., McLennan, S.M., 1995. The Geochemical Evolution of the Continental Crust. Rev. Geophys. 33 (2), 241–265.

Ubide, T., Mollo, S., Zhao, J., Nazzari, M., Scarlato, P., 2019. Sector-Zoned Clinopyroxene as a Recorder of Magma history, Eruption Triggers, and Ascent rates. Geochim. Cosmochim. Acta 251, 265–283.

Uçurum, A., 2000. Listwaenites in Turkey: Perspectives on Formation and precious Metal Concentration with Reference to Occurrences in East-Central Anatolia. Ofioliti 25 (1), 15–29.

Uçurum, A., Larson, L.T., Boztug, D., 1996. Geology, Geochemistry, and Petrology of the Alkaline Subvolcanic Trachyte-Hosted Iron Deposit in the Karakuz Area, Northwestern Hekimhan-Malatya, Turkey. Int. Geol. Rev. 38 (11), 995–1005.

Uyeda, S., Kanamori, H., 1979. Back-arc opening and the Mode of Subduction. J. Geophys. Res. 84 (B3), 1049–1061.

Uysal, I.T., Feng, Y., Zhao, J., Altunel, E., Weatherley, D., Karabacak, V., Cengiz, O., Golding, S.D., Lawrence, M.G., Collerson, K.D., 2007. U-Series Dating and Geochemical Tracing of Late Quaternary Travertine in Co-Seismic Fissures. Earth Planet. Sci. Lett. 257 (3–4), 450–462.

Uysal, I.T., Feng, Y., Zhao, J., Bolhar, R., Işik, V., Baublys, K.E., Yago, A., Golding, S.D., 2011. Seismic Cycles Recorded in Late Quaternary Calcite Veins: Geochronological, Geochemical and Microstructural evidence. Earth Planet. Sci. Lett. 303 (1–2), 84–96.

Veizer, J., Ala, D., Azmy, K., Bruckschen, P., Buhl, D., Bruhn, F., Carden, G.A., Diener, A., Ebneth, S., Godderis, Y., Jasper, T., 1999. 87Sr/86Sr, δ13C and δ18O evolution of Phanerozoic seawater. Chemical geology 161 (1-3), 59–88.

Vidal, N., Merle, O., 2000. Reactivation of Basement Faults beneath Volcanoes: A New Model of Flank Collapse. J. Volcanol. Geotherm. Res. 99 (1–4), 9–26.

Vignaroli, G., Berardi, G., Billi, A., Kele, S., Rossetti, F., Soligo, M., Bernasconi, S.M., 2016. Tectonics, Hydrothermalism, and Paleoclimate Recorded by Quaternary Travertines and their Spatio-Temporal distribution in the Albegna Basin, Central Italy: Insights on Tyrrhenian margin Neotectonics. Lithosphere 8 (4), 335–358.

Wei, X., Xu, Y.G., Feng, Y.X., Zhao, J.X., 2014. Plume-lithosphere interaction in the generation of the Tarim large igneous province, NW China: geochronological and geochemical constraints. Am. J. Sci. 314, 314–356.

Wheat, C.G., Seewald, J.S., Takai, K., 2020. Fluid transport and reaction processes within a serpentinite mud volcano: South Chamorro Seamount. Geochim. Cosmochim. Acta 269, 413–428.

Woodhead, J., Hellstrom, J., Paton, C., Hergt, J., Greig, A., Maas, R., 2008. A Guide to Depth Profiling and Imaging applications of LA-ICP-MS. In: Laser Ablation ICP–MS in the Earth Sciences: Current Practices and Outstanding Issues, 40.